MNRAS **000**, 1–13 (2023) Preprint 17 January 2023 Compiled using MNRAS LATEX style file v3.0

High-precision photometric and high-resolution spectroscopic characterisation of HD 180347

Otto Trust[1]★, Lyudmila Mashonkina[2], Edward Jurua[1], Peter De Cat[3], Vadim Tsymbal[2], and Santosh Joshi[4]

[1]*Department of Physics, Mbarara University of Science and Technology, P.O. Box 1410, Mbarara, Uganda*
[2]*Institute of Astronomy, Russian Academy of Sciences, 119017, Pyatnitskaya str., 48, Moscow, Russia*
[3]*Royal Observatory of Belgium, Ringlaan 3, B-1180 Brussel, Belgium*
[4]*Aryabhatta Research Institute of Observational Sciences, Manora Peak, Nainital- 263002, India*

Accepted XXX. Received YYY; in original form ZZZ

ABSTRACT

We report the analysis of high-precision space-based photometric and high-resolution spectroscopic observations of HD 180347. The high-quality light curves from the Transiting Exoplanet Survey Satellite (*TESS*) under sectors 14, 15, and 26 were used. By visual inspection of the light curves and the Fourier transforms, only low-frequency signals (less than 1 d^{-1}) were detected. After using wavelet, autocorrelation, and composite spectrum analyses, HD 180347 is classified as a rotational variable with a period of about 4.1 ± 0.17 days. In reference to the observation limit of *TESS*, no pulsations were detected. For the spectroscopic analysis, we used data collected with the High Efficiency and Resolution Mercator Échelle Spectrograph (HERMES) spectrograph mounted at the Cassegrain focus of the 1.2-m Mercator telescope located at La Palma, Spain. We determined the spectral type of this star and obtained atmospheric parameters such as the effective temperature, the surface gravity, and the projected rotational, microturbulent, and radial velocities. We also performed a detailed individual chemical abundance analysis for the target star. Based on the spectral classification analysis and chemical abundance pattern, we classify this star as Am (kA1hA8mA8). NLTE abundance analysis for Na I, Mg I-II, Si I-II, Ca I-II, Sr II, and Ba II indicates an average abundance correction (Δ) of 0.49 dex, 0.05 dex, 0.19 dex, 0.02 dex, 0.01 dex, and 0.34 dex, respectively. We report that Na I 588.995, 589.592 nm, Mg I 518.360 nm, Mg II 448.115 nm, Si II 634.711, 637.137 nm, Ba II 455.403, 493.408, 614.171, and 649.690 nm are found to be more sensitive to NLTE effects.

Key words: stars: chemically peculiar – stars: rotation – stars: starspots – stars: general – HD 180347

1 INTRODUCTION

Over 10% of the intermediate mass main-sequence stars (A- and F-type) are chemically peculiar (CP). The CP stars show anomalies in their chemical composition compared to the solar one. The CP stars are categorised into four major groups: CP1 stars (the metallic-line or Am/Fm stars), CP2 stars (the magnetic Ap stars), CP3 stars (the Mercury-Manganese or HgMn stars) and CP4 stars (the He-weak stars), based on their magnetic field and absorption line strengths (Preston 1974). The Am stars are distinguished by low abundances of some elements such as Ca and Sc, as well as an excess of Fe-group metals and often weak or absent magnetic fields (Conti 1970; Preston 1974; Romanyuk 2007). In the Am stars subgroup, the Ca II K-line appears too early compared to the types derived from hydrogen lines, whilst metallic lines appear too late, resulting in spectral types inferred from the Ca II K- and metal lines differing by five or more spectral subclasses. For the marginal Am stars, the spectral subclasses between the Ca II K- and metal lines are less than five. The frequently used detailed classification for this class of objects involves three spectral subtypes prefixed with k, h, and m, which represent Ca II K-line, hydrogen lines, and metallic lines, respectively.

Some metals like Si, Cr, Sr, and Hg, as well as rare-earth elements like Eu, Nd, Pr, and others, are overabundant in the CP2 stars in comparison to solar values (Conti 1970; Preston 1974; Kurtz & Martinez 2000; Romanyuk 2007). Unlike CP1 and CP3, the presence of well-organized magnetic fields with strengths of several tens of kG is also a feature of CP2 stars (Aurière et al. 2007). In their spectra, the CP3 stars have amplified HgII (398.4 nm) and/or MnII lines, as well as faint lines of light elements (such as He, Al, and N). In the spectra of the CP4 stars, there are unusually weak HeI lines and these stars are characterised by magnetic fields with a strength of up to 1 kG (Jones & Wolff 1974; Preston 1974; Smith 1997; Bohlender et al. 1998). The CP stars are slow rotators

★ E-mail: otrust@must.ac.ug

with a projected rotational velocity ($v \sin i$) below 120 km s^{-1} (Abt 2009).

The interplay between radiative levitation and gravitational settling, known as atomic diffusion, is assumed to be the principal source of chemical anomalies in CP stars (Michaud 1970; Watson 1970; Khokhlova 1981; Hui-Bon-Hoa 2000; Richer et al. 2000; Turcotte 2003; Théado et al. 2011). In the absence of mixing, light elements sink under gravity and are perceived as underabundant, whereas heavy elements are radiatively forced outward and reflected as over-abundant. This idea necessitates calm and stable atmospheres, which are aided by CP stars' sluggish rotation behavior (Takeda et al. 2008; Fossati et al. 2008; Stateva et al. 2009; Abt 2009) and Ap stars' strong magnetic fields. Strong magnetic fields are expected to stabilize convective material, but slow rotation reduces meridional circulation and, as a result, reduces mixing, which would prevent atomic diffusion. The physical processes that are active in CP stars, such as pulsation (Dziembowski et al. 1988; Soufi et al. 1998) and convective overshooting (Browning et al. 2004; Costa et al. 2019), and their chemical abundances (Turcotte 2001; Murphy 2014) are heavily influenced by rotation.

Renson & Manfroid (2009)'s General Catalogue of Ap and Am stars has 8205 peculiar (or suspected peculiar) stars, making it one of the most comprehensive catalogues of peculiar stars. There are 3652 (candidate) Ap stars, 162 (candidate) HgMn stars, 4299 (candidate) Am stars, and 92 stars that have been incorrectly catalogued as Ap, HgMn, or Am at least once. HD 180347 (= TIC 298969563 = KIC 12253106) is one of the probable Am stars in the General Catalogue of Ap and Am stars by Renson & Manfroid (2009).

Smalley et al. (2011) found HD 180347 to be variable with amplitude less than 0.01 mmag. Later on, Balona et al. (2015) classified the variability as rotational with a period of 4.1 days using data of the nominal *Kepler* mission (Borucki et al. 2010). Recently, Catanzaro et al. (2019) reported HD 180347 among possible pulsators. However, based on the diffusion theory, the He II ionisation zone, which excites δ Scuti-type pulsations, should be absent in Am stars. Therefore, it is important to perform a detailed and homogeneous classification and variability study of such a star.

To search and study the pulsational variabilities in Ap and Am/Fm stars, a dedicated ground-based project the "Nainital-Cape Survey" was initiated between astronomers of India and South Africa. However, with time, astronomers from other institutions in other countries joined this programme, transforming it into a multinational collaborative project and a number of results are published (e.g; Ashoka et al. 2000; Martinez et al. 2001; Joshi et al. 2003, 2006, 2009, 2010, 2012, 2016, 2017; Trust et al. 2020, 2021; Joshi et al. 2022). In this paper, we study HD 180347 using data in the *TESS* archive supplemented with high-resolution spectroscopic data from HERMES and spectrophotometric observations available to the public in various databases. The aim of the study is to investigate the photometric variability and fully characterise the candidate Am star HD 180347.

This paper is organised as follows. The spectroscopic observations and data reduction are discussed in Section 2. *TESS* photometry is given in Section 3. Spectral classification is presented in Section 4, while fundamental parameters and individual chemical abundance analyses are given in Section 5 and 6, respectively. Finally, the conclusions are given in Section 7.

2 OBSERVATIONS AND DATA REDUCTION

A high-resolution spectroscopic observation of HD 180347 was done on the night of 6 November 2018, using HERMES (Raskin et al. 2011) mounted at the Cassegrain focus of the 1.2-m Mercator telescope located at La Palma, Spain. This star was observed for a total exposure time of 13.3 minutes. This spectrograph records optical spectra in the wavelength (λ) range of 377 to 900 nm spanning 55 spectral orders in a single exposure. This instrument has a resolving power of 85 000 in high-resolution mode, with a radial velocity stability of roughly 50 m s^{-1} and an outstanding throughput (Raskin et al. 2011).

The spectrum was reduced using the dedicated HERMES pipeline following the usual reduction procedure for échelle spectra, including subtraction of bias and stray light, flat-field correction, order-by-order extraction, wavelength calibration frames with Thorium-Argon lamps, removal of cosmic rays, and merging of the orders. This procedure resulted in a spectrum with a signal-to-noise ratio (SNR) of 108, 119, and 76 at λ = 500, 650, and 810 nm, respectively. The spectrum was manually normalized up to the local continuum using an integrated program ISPEC (Blanco-Cuaresma et al. 2014; Blanco-Cuaresma 2019). Finally, we corrected for barycentric motion in the spectrum. The barycentric Julian date of the observed high-resolution spectrum is BJD 2458429.3586322.

3 *TESS* DATA PHOTOMETRY

We used the 2-min cadence light curves obtained with *TESS* (Ricker et al. 2015) from 18 July 2019 to 14 August 2019 (sector 14), 15 August 2019 to 10 September 2019 (sector 15), and 9 June 2020 to 4 July 2020 (sector 26) to search for signatures of rotational modulation and/or stellar pulsations. The light curves using presearch data conditioning (PDC) were selected (PDCSAP_SAP flux column in the FITS file). These are corrected for time-correlated instrumental signatures (Jenkins et al. 2016) and good enough for our analysis.

The PDC data, as given in the FITS files downloaded from the Barbara A. Mikulski Archive for Space Telescopes (MAST)[1], were used. In constructing the final light curves, the mean flux was subtracted from each individual flux measurement. The result was divided by the mean flux and multiplied by 1087.5 for the conversion to millimagnitudes (mmag). Our classification of variability is based on the General Catalog of Variable Stars (GCVS, Kazarovets et al. 2017).

We calculated the amplitude SNR value for candidate signal peaks in the Fourier transform (Lenz & Breger 2005) to detect significant signal peaks, using a smoothing function across the frequency spectrum to calculate the noise spectrum (Breger et al. 1993). The amplitude of a significant peak exceeds the background noise by a factor of four or more. Simulations, as detailed in Koen (2010), support this significance criterion. Furthermore, Frescura et al. (2008) noted the subjectivity of determining the noise level when calculating the SNR. We augment the SNR approach by calculating the false-alarm probability (FAP) for each peak using the independent frequency method reported in VanderPlas (2018). This criterion calculates the likelihood that a peak was caused by noise rather than an inherent signal. The lower the FAP value, the more likely it is that a given peak is real. A threshold FAP of 10^{-8} (Joshi et al. 2022) was adopted across all the *TESS* data sets. This threshold is also

[1] https://mast.stsci.edu/portal/Mashup/Clients/Mast/Portal.html

noted by Bowman et al. (2018) to be particularly significant at low frequencies. The detected signals are represented by blue lines in Fig. 1 and their properties are listed in Table 1. The errors listed in this table were determined using a least-square algorithm.

By visual inspection of the Fourier transforms in Fig. 1, only long-period signals (more than 1 d) were detected. For sectors 14 and 26, the frequency values given in Table 1 seem to be consistent with frequencies + harmonic scenario, which suggests spot-induced rotational modulation. In the presence of the harmonic, the rotational frequency is represented by the fundamental. It is possible that the fundamental in some stars is missing or has a very low amplitude, causing the most significant period to be half that of the genuine rotational period. This could happen in stars with two almost equal-sized diametrically positioned spots (or spotted regions). Based on the Fourier transforms in Fig. 1, HD 180347 could be a typical example of such a case.

Low-level eclipses and rotational signals can be confused. In order to avoid this, the rotational variability identification is limited to stars with amplitudes of less than 10 mmag. To increase the confidence of the variability type of this star, we performed wavelet, autocorrelation functions (ACFs), and composite spectrum analyses of the available *TESS* time series data.

3.1 Wavelet analysis

Star spots could be the cause of the detected signals in the time series data. Star spots, like sunspots, are well-known tracers of stellar rotation, but their dynamic behaviour can also be used to study other phenomena like stellar magnetic activity and cycles (García et al. 2010; Mathur et al. 2014). Sunspots change in size and location over time. Sunspots can appear or disappear at any time. If A-type star spots are comparable to sunspots, one might expect them to behave similarly. Variations in the amplitude of the frequencies are caused by variations in the size and location of starspots. To investigate the frequency change, we created time-frequency diagrams for the *TESS* data sets using the wavelet technique, which allows for a better interpretation of physical features (such as spots) before they are considered for period determination (Torrence & Compo 1998; Mathur et al. 2010).

This technique allows for the analysis of non-stationary signals for a given signal. The reference wavelet was the Morlet wavelet, which is interpreted as the convolution of a sinusoidal and a Gaussian function (Goupillaud et al. 1984; Holschneider et al. 1989). The Morlet wavelet has several advantages: (i) it is Gaussian-shaped in the frequency domain, which minimizes ripple effects that can be misinterpreted as oscillations; (ii) the results of Morlet wavelet convolution retain the original signal's temporal resolution; and (iii) wavelet convolution is computationally efficient.

For each frequency, we calculated the correlation between the mother wavelet and the data. This was accomplished by moving the wavelet along the time axis of the light curves, producing a wavelet power spectrum (WPS). The global wavelets power spectrum (GWPS) was then generated by projecting the WPS along the period axis. Panel (c) of Figs. 2, 3, and 4 show the time-frequency plots of the time series from *TESS* observation sectors 14, 15, and 26, respectively. The blue and black colours in the WPS denote low and high-power regions, respectively. By visual inspection of the GWPS's shown in panel (d) of Figs. 2, 3, and 4, we report rotational periods of 4.10 ± 0.44 d, 3.54 ± 0.45 d, and 4.10 ± 0.45 d, respectively. Within error limits, these results are consistent with those obtained directly from periodograms in Fig. 1.

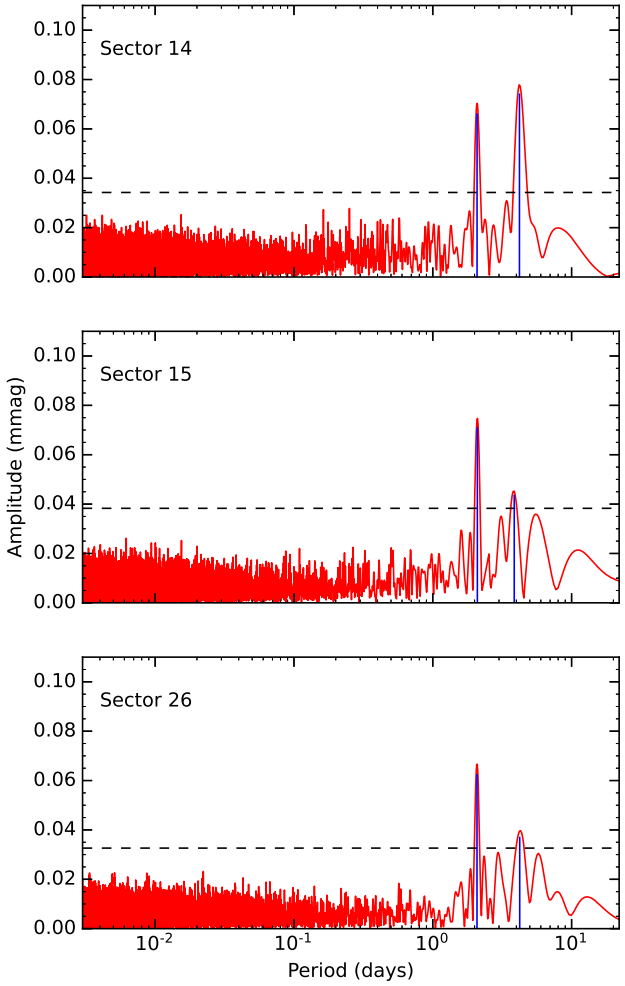

Figure 1. Linear-log periodogram distribution of spectral amplitudes, in mmag, derived from applying the Fourier transform algorithm to the light curves from each sector (*given in the top left corner of each panel*). The *blue lines* in the respective panels show the detected signals. The *black dashed lines* represent the threshold false alarm probability of 10^{-8}, and the peaks above this line are considered significant signals.

3.2 Autocorrelation functions

The ACFs show how similar light-curves are to themselves at certain time differences (McQuillan et al. 2013, 2014). Briefly, the autocorrelation function (ACF) is given by:

$$ACF_{\tau} = \frac{1}{N} \frac{\sum_{i=1}^{N} (x(t_i) - \bar{x})(x(t_i - \tau) - \bar{x})}{\sigma^2}, \quad (1)$$

where τ is the lag time shift between the same time-series, $x(t_i)$ is the time-series value at time t_i, $\bar{x}$ is the temporal mean of the time series, and σ^2 is the time-series variance. The variance is given by:

$$\sigma^2 = \frac{\sum_{i=1}^{N} (x(t_i) - \bar{x})^2}{N}. \quad (2)$$

At time lag shift between the time series, $\tau = 0$, the ACF in Eq. 1 reduces to:

$$ACF_{\tau=0} = \frac{1}{N} \frac{\sum_{i=1}^{N} (x(t_i) - \bar{x})^2}{\sigma^2}. \quad (3)$$

Table 1. Properties of signals detected in the *TESS* data obtained in three different sectors 14, 15, and 26. Listed is the frequency, period, amplitude, phase, probability of false alarm ($\log_{10}$(FAP)), and signal-to-noise ratio (SNR) as determined from the Fourier transforms.

TESS Observation Sector	Frequency (d^{-1})	Period (d)	Amplitude (mmag)	Phase (rad)	$\log_{10}$(FAP)	SNR
14	0.2375 ± 0.0015	4.211 ± 0.027	0.079 ± 0.006	-1.72 ± 0.07	-37	21
	0.4798 ± 0.0016	2.084 ± 0.007	0.077 ± 0.006	1.41 ± 0.08	-32	19
15	0.4775 ± 0.0018	2.094 ± 0.008	0.074 ± 0.006	-0.80 ± 0.08	-33	19
	0.2589 ± 0.0031	3.862 ± 0.046	0.043 ± 0.006	1.85 ± 0.13	-9	12
26	0.4803 ± 0.0017	2.082 ± 0.007	0.062 ± 0.005	-2.69 ± 0.08	-32	19
	0.2365 ± 0.0029	4.228 ± 0.052	0.042 ± 0.005	2.49 ± 0.12	-9	12

A comparison of Eqs. 2 and 3 results in $ACF_{\tau=0} = 1$. When a time series contains a dominant repeated signal of the period ($P_{\rm ACF}$), probably created by the presence of spots, the pattern is expected to anti-correlate and correlate such that $ACF_{\tau=kP_{\rm ACF}/2} = -1$ and $ACF_{\tau=kP_{\rm ACF}} = 1$, respectively, where $k = 1, 2, 3, 4, ..., m$ and $mP_{\rm ACF} < t_N$. However, this is not the case when the whole time-series is correlated with itself due to limited overlap, for any time-lag not equal to zero. The ACF oscillates between maximum and minimum values as the patterns become correlated and anti-correlated, and the amplitude decreases as the overlap decreases. The overall amplitude of ACFs can additionally be reduced due to variations of signals in the time series, which could be the reflection of variations in the size of the spot (active region). Therefore, at time lags greater than zero, the ACF resembles a displacement of an under-damped simple harmonic oscillator (uSHO), (Giles et al. 2017)

$$y(\tau) = e^{-\tau/\tau_{\rm DT}} \left({\rm A} \cos\left(\frac{2\pi\tau}{P_{\rm ACF}}\right) + {\rm B} \cos\left(\frac{4\pi\tau}{P_{\rm ACF}}\right) + y_0 \right), \quad (4)$$

where

$\tau = \Delta T \times {\rm n}$,

ΔT is the median time difference of the light-curve, n ascends from 0 to the total number of ACFs, y(τ) is the ACF, $\tau_{\rm DT}$ is the decay-time scale of the ACF, $P_{\rm ACF}$ is the time lag corresponding to the first maximum of the ACF that represents the rotation period of the star, and A, B, and y_0 that do not represent any physical stellar properties but are constants that are needed in the fit of an uSHO. We performed an ACFs analysis of the time series and obtained values of $P_{\rm ACF}$ of 4.1 d, 2 d, and 1.98 d, for sectors 14, 15, and 26, respectively. In panel (e) of Fig. 2, the ACF shows sub-peaks are at $\tau = kp/2$. This is thought to occur when slightly weaker spotted regions are diametrically opposed to the dominant spotted region as earlier mentioned in Section 3.

3.3 Composite spectrum

We created a composite spectrum (CS) by combining the ACF and normalized GWPS (Ceillier et al. 2015; Ceillier et al. 2017). The CS is very sensitive to the periods detected in both ACF and GWPS, which makes it reliable up to about 95% of the time (Aigrain et al. 2015). We calculated the period, $P_{\rm CS}$, by fitting the peaks in the CS with a Gaussian function. The associated uncertainty corresponds to the peak's half width at half maximum (HWHM). By visual inspection of panel (f) of Figs. 2, 3, and 4, we report rotational periods of 4.10 ± 0.17 d, 4.10 ± 0.16 d, and 4.10 ± 0.15 d, respectively.

4 SPECTRAL CLASSIFICATION

We used the MK classification system (Morgan et al. 1943; Gray & Corbally 2009) to perform a spectral classification analysis on HD 180347. It can be used to determine the chemical peculiarity of a star (Gray & Corbally 2009). The spectral type and luminosity class are determined by comparing the observed spectra to well-known standards while accounting for crucial hydrogen and metal lines. We used the spectral energy distribution (SED) and the high-resolution HERMES spectrum to do the spectral classification of HD 180347.

4.1 Spectral classification from SED

SEDs are created by combining spectrophotometry obtained at various wavelengths, ideally from ultraviolet to infrared. We used version 7.0 of the VOSA (Bayo et al. 2008) to automatically search for spectrophotometric observations in various databases, including the Johnson (Johnson & Morgan 1953; Oja 1985), TychoII (Høg et al. 2000), 2MASS (Skrutskie et al. 2006), WISE (Wright et al. 2010), and GAIA DR2 (Evans et al. 2018) catalogues. We determined the reddening parameter $E({\rm B-V})$ from 3D models (Green 2018; Green et al. 2019) using the GAIA parallaxes (Evans et al. 2018) and the stellar galactic coordinates from the SIMBAD database[2] (Wenger et al. 2000) and found a value of 0.0173 ± 0.0015 mag. To deredden the SED, we used the extinction law originally developed by Fitzpatrick (1999) and further improved by Indebetouw et al. (2005) in the infrared. The SED of HD 180347 is represented by filled circles in Fig. 5. We used the VOSA package to cross-match it with the template libraries created by Kesseli et al. (2017) from spectra of the Sloan Digital Sky Survey (SDSS; York et al. 2000). It uses a least-squares minimisation approach and results in a classification as an A9 dwarf, indicating that HD 180347 would be a main-sequence star. The uncertainty on the spectral type is approximately three spectral subclasses.

4.2 Spectral classification from spectroscopy

The HERMES spectrum of HD 180347 was classified with the help of the code MKCLASS (Gray & Corbally 2014) in combination with the standard libraries given by Gray et al. (2003). The spectra of this library were obtained with the 0.8-m telescope of the Dark Sky Observatory (DSO) in the northwest of North Carolina (USA) by using the Gray/Miller classification spectrograph with a grating having either 600 or 1200 grooves/mm^{-1}. The standard spectra

[2] https://simbad.u-strasbg.fr/simbad/

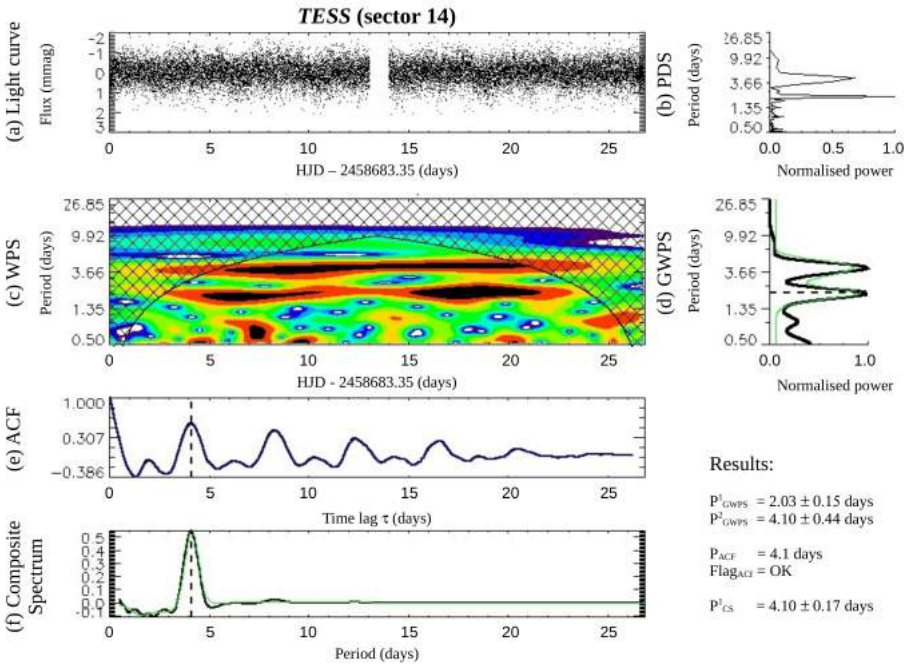

Figure 2. Search for the rotation period of HD 180347 based on the *TESS* data from sector 14. Panel (a) shows the light curve while the power density spectrum (PDS) as a function of the period between 0.5 and 27 d is given in panel (b). The wavelet power spectrum (WPS) computed using a Morlet wavelet between 0.5 and 27 d on a logarithmic scale is shown in panel (c) and the associated global wavelet power spectrum (GWPS) is given in panel (d). The colours black and blue represent high and low power, respectively. The autocorrelation function (ACF) of the full light curve and the composite spectrum (CS) (Ceillier et al. 2015; Ceillier et al. 2017), plotted between 0 and 27 d, are presented in panels (e) and (f), respectively. The cone of influence corresponding to the unreliable results is represented by the black-crossed area in the WPS. The automatically detected rotational period estimates are denoted by the black dashed lines. A summary of the results is given in the bottom right corner. The quality flag $\mathrm{Flag_{ACF}}$ indicates whether the selected P_{ACF} corresponds to the dominant of the regularly spaced peaks of the ACF.

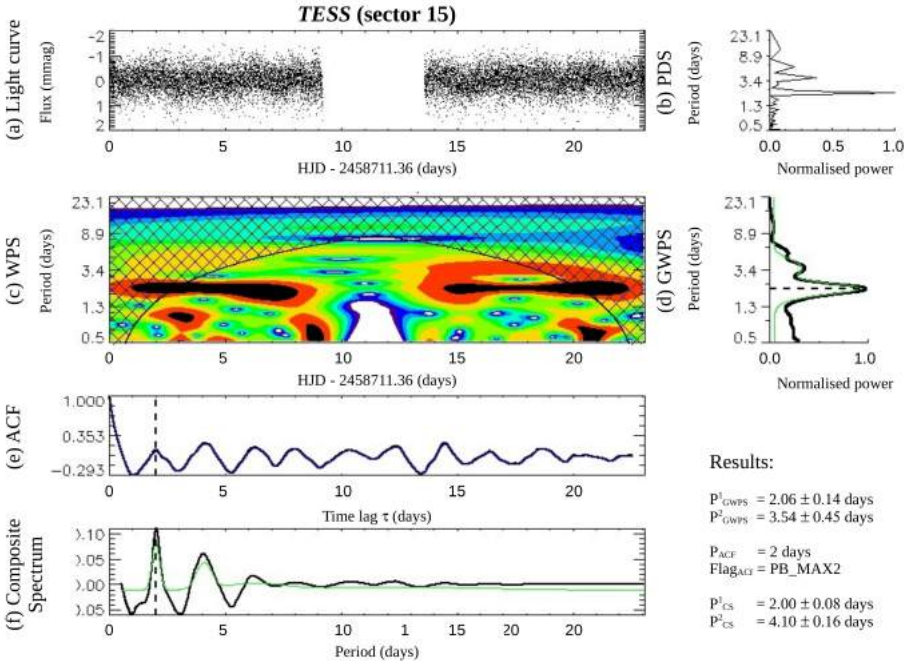

Figure 3. Same as Fig. 2 but for the *TESS* data from sector 15.

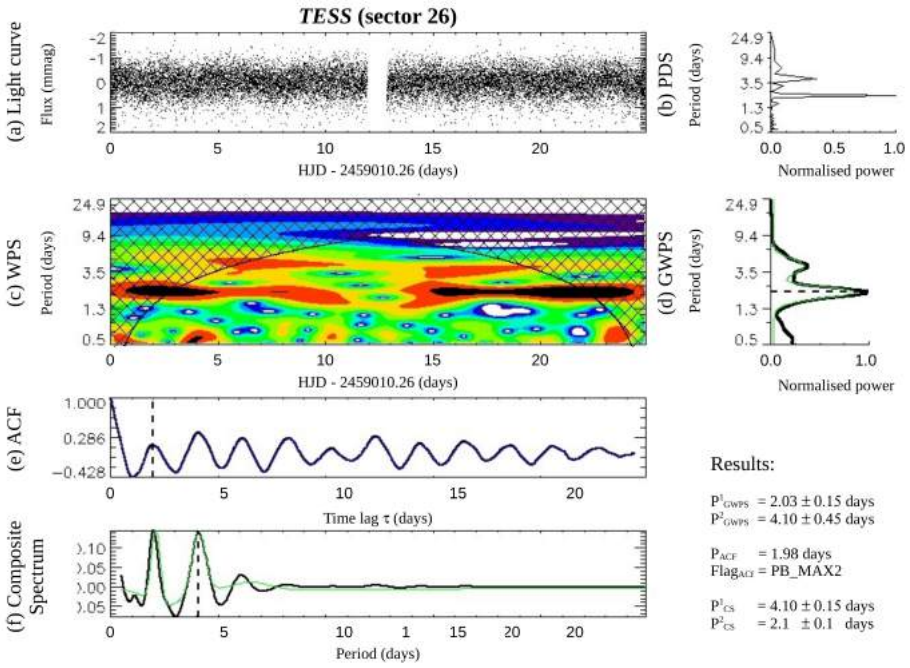

Figure 4. Same as Fig. 2 but for the *TESS* data from sector 26.

span the violet-green wavelength region at a resolution range of 0.18 –0.36 nm / 2 pixels (Gray & Corbally 2014).

Our HERMES spectrum is not observed with the same spectrograph/grating combination as the spectra of the standard library. We, therefore, truncated its wavelength region, re-binned it, and convoluted the spectrum with a gaussian of appropriate full width at half maximum of 0.16 nm to match the specifications of the standards as closely as possible.

We used the metric-distance technique (LaSala 1994), which is based on a weighted least-square comparison of the program spectrum with that of the MK standard stars (Gray & Corbally 2014), to determine the spectral type based on (i) hydrogen lines (Hγ and Hσ), (ii) metal lines, and (iii) the Ca II K-line. For a chemically normal star, this should lead to the same results while different spectral types in these three regions are expected in the case of a chemically peculiar star (Gray & Corbally 2009). With this method, we found a spectral type of kA1hA8mA8, confirming the classification of HD 180347 as an Am star, first reported by Bidelman (1985).

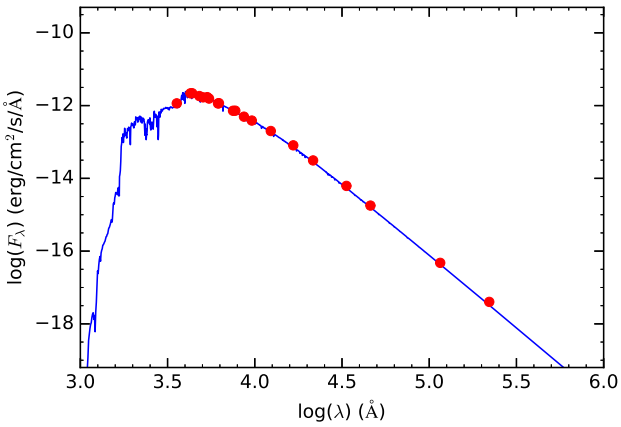

Figure 5. The red filled circles represent the SED of HD 180347. The blue solid line represents the best fit to the data obtained using the VOSA tool.

5 FUNDAMENTAL STELLAR PARAMETERS

High-resolution spectroscopy is a robust method to derive accurate values of the basic stellar parameters like the effective temperature ($T_{\rm eff}$), surface gravity ($\log g$), and metallicity ([M/H]) (Section 5.1). Once they are known, they can be used to calculate values of additional fundamental stellar parameters (Section 5.2).

5.1 Derived stellar parameters

To achieve convergence during synthesis, knowledge of a good initial guess for the basic stellar parameters is critical. Therefore, we derived $T_{\rm eff}$, $\log g$, and [M/H] in two steps.

In the first step, the SED of HD 180347 was used to obtain preliminary values for $T_{\rm eff}$, $\log g$, and [M/H]. Using the VOSA tool and the ATLAS9 Kurucz ODFNEW/NOVER models (Castelli & Kurucz 2003), we performed a least-square fit to the SED to obtain $T_{\rm eff}$, $\log g$, and [M/H] as 7750 ± 250 K, 4.0 ± 0.5 cm s^{-2}, and 0.5 ± 0.30 dex, respectively. The best model is represented by a blue line in Fig. 5.

In the second step, the HERMES spectrum was used to derive the radial velocity ($v_{\rm rad}$; Section 5.1.1), $v \sin i$ (Section 5.1.2), and the microturbulent velocity (ξ) and final values of $T_{\rm eff}$, $\log g$ and [M/H] (Section 5.1.3).

5.1.1 *Radial velocity*

We calculated the radial velocity $v_{\rm rad}$ by computing the cross correlation function (CCF) with various pre-selected masks created from line lists using the code ISPEC. We found a $v_{\rm rad}$ value of

$9.3 \pm 0.3\,\mathrm{km\,s^{-1}}$ corresponding to the time that the HERMES spectrum was observed (BJD 2458429.3586322).

5.1.2 *Projected rotational velocity*

Using the initial values from the SED analysis, $v \sin i$ was calculated by comparing the observed spectrum to a grid of synthetic spectra. The least-square method was used in this comparison, which was based on the MINUIT minimization software, which is included in the GIRFIT package (Frémat et al. 2006). We interpolated the spectrum in a grid of stellar fluxes computed using plane-parallel ATLAS9[3] model atmospheres (Castelli & Kurucz 2003) for $T_{\rm eff}$, $\log g$, and $v_{\rm rad}$ values of 7750 K, $4.0\,\mathrm{cm\,s^{-2}}$, and $9.3\,\mathrm{km\,s^{-1}}$, respectively, and varied $v \sin i$ values in the range $0-100\,\mathrm{km\,s^{-1}}$ with steps of $1\,\mathrm{km\,s^{-1}}$. We used the spectral region with the Mg I triplet (516 – 519 nm). With this method, the resulting value for $v \sin i$ is $14 \pm 2\,\mathrm{km\,s^{-1}}$.

5.1.3 *Effective temperature, surface gravity, metallicity, and microturbulent velocity*

We determined $T_{\rm eff}$, $\log g$, [M/H], and ξ by synthesizing stellar spectra with the MOOG radiative transfer code (Sneden et al. 2012). We used the ATLAS9 model atmospheres, the Vienna Atomic Line Database (VALD) line list (Kupka et al. 1999), and the solar abundances of Asplund et al. (2009), all of which were combined in the integrated software package ISPEC. $T_{\rm eff}$ and $\log g$ were estimated from the hydrogen line profiles and Fe I/Fe II lines, respectively. [M/H] was determined from all available lines, with Fe, Ca, and Ti lines dominating. Since $v \sin i$ is low, the ξ was determined by fitting Fe and Ti II lines and its initial guess was calculated from the relation (Gebran et al. 2014),

$$\xi = 3.31 \times \exp\left[-\left(\log\left(\frac{T_{\rm eff}}{8071.03}\right)^2 / 0.01045\right)\right]. \quad (5)$$

The resulting values are 7740 ± 170 K for $T_{\rm eff}$, $3.98 \pm 0.12\,\mathrm{cm\,s^{-2}}$ for $\log g$, 0.11 ± 0.08 dex for [M/H], and $3.81 \pm 0.12\,\mathrm{km\,s^{-1}}$ for ξ.

Fig. 6 shows the Hβ (*top left*), Mg I triplet (*bottom*), and Hα (*top right*) line regions for the HERMES spectrum of HD 180347 (*black*) and the synthetic (*red*) spectra computed with the final values of the atmospheric parameters as listed in the top part of Table 2. Within the error limits, our results agree with those from previous studies (e.g. McDonald et al. 2012, Catanzaro et al. 2015, Mathur et al. 2017, Andrae et al. 2018, and Murphy et al. (2019)).

5.2 Calculated stellar parameters

5.2.1 *Luminosity and radius*

Based on the standard technique, we determined the luminosity ($\log(L_\star/L_\odot)$) (cf. Trust et al. 2021). Extinction was calculated as described in Section 4.1. Using the temperature dependent function by Flower (1996) revised by Torres (2010), the bolometric correction (BC) was calculated. We computed the absolute magnitude ($M_{\rm V}$) using GAIA parallaxes (Evans et al. 2018). Uncertainties in V-band indices, parallax, and $T_{\rm eff}$ contribute to the uncertainties in $\log(L_\star/L_\odot)$. We used the method described in Trust et al. (2021) to calculate the stellar radius ($R_\star$) from the Stefan–Boltzmann law (Boltzmann 1884; Paul et al. 2015; Montambaux 2018). The procedure produced a $M_{\rm V}$ value of 2.252 ± 0.083 mag, a BC value of 0.0283 ± 0.0055 mag, a $\log(L_\star/L_\odot)$ value of 0.993 ± 0.030, and a $R_\star$ value of $1.75 \pm 0.14\,\mathrm{R_\odot}$. Within the error limits, our results are in agreement with those reported in Andrae et al. (2018).

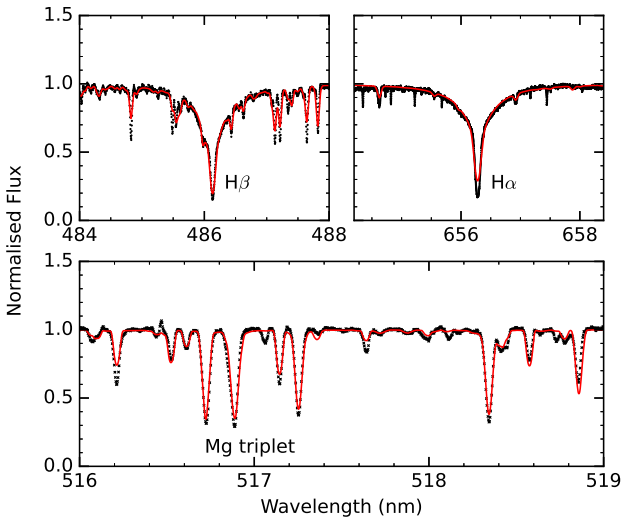

Figure 6. The Hβ (*top left*), Mg I triplet (*bottom*), and Hα (*top right*) line regions for the target star. The observed (*black*) and synthetic spectra (*red*) are shown. The synthetic spectrum was obtained with LTE consideration. The majority of the narrow features in the observed spectrum that are not fit by the models are telluric lines.

Table 2. Overview of the values of fundamental parameters of HD 180347 resulting from this study. The top part lists the parameters directly obtained from the HERMES spectrum while the bottom part gives those that were derived from them.

Parameter	Value	Error
$T_{\rm eff}$ (K)	7740	170
$\log g$ ($\mathrm{cm\,s^{-2}}$)	3.98	0.12
[M/H] (dex)	0.11	0.08
ξ ($\mathrm{km\,s^{-1}}$)	3.81	0.12
$v \sin i$ ($\mathrm{km\,s^{-1}}$)	14	2
$v_{\rm rad}$ ($\mathrm{km\,s^{-1}}$)	9.3	0.3
$\log(L_\star/L_\odot)$	0.993	0.030
$R_\star$ ($\mathrm{R_\odot}$)	1.75	0.14
$v_{\rm eq}$ ($\mathrm{km\,s^{-1}}$)	22	1
i (°)	40	5
$M_\star$ ($\mathrm{M_\odot}$)	1.74	0.23
age (Gyr)	0.85	0.18

5.2.2 *Equatorial rotational velocity and inclination angle*

Using the rotational period (4.10 ± 0.17 days) obtained from the *TESS* data and the value of $R_\star$, the equatorial rotational velocity $v_{\rm eq}$ was calculated (cf. Trust et al. 2020). We constrained the inclination angle (i) from the relationship between $v \sin i$ and the equatorial rotational velocity ($v_{\rm eq}$). We report the values of $v_{\rm eq}$ and i to be $22 \pm 1\,\mathrm{km\,s^{-1}}$ and $40 \pm 5°$, respectively.

[3] http://www.stsci.edu/hst/observatory/crds/castelli_kurucz_atlas.html

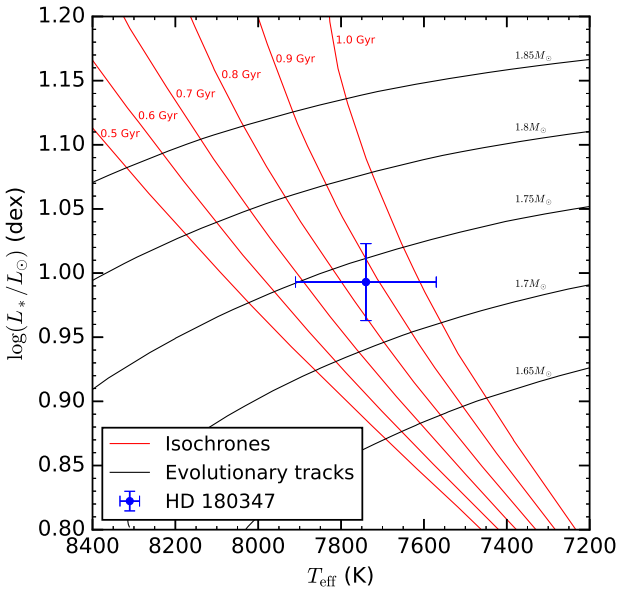

Figure 7. The HR diagram showing the position of HD 180347 relative to a number of the PARSEC 1.2 evolutionary tracks (*black solid lines*) and isochrones (*red solid lines*) (Bressan et al. 2012).

5.2.3 *Stellar mass and age*

Using the $T_{\rm eff}$ and $\log(L_\star/L_\odot)$ values derived in the previous sections, the stellar mass ($M_\star$) and age were determined by interpolating the PARSEC 1.2 evolutionary tracks and isochrones (Bressan et al. 2012), respectively. The grids of evolutionary tracks span a mass range of $1.5-2.5\,M_\odot$ while the isochrones have ages ranging between 0.2 and 1 Gyr. The results for $M_\star$ and age are $1.74\pm0.23\,M_\odot$ and 0.85 ± 0.18 Gyr, respectively. Fig. 7 represents a Hertzsprung–Russell (HR) diagram showing the position of HD 180347 relative to a number of the PARSEC 1.2 evolutionary tracks and isochrones.

The values of the fundamental parameters derived in this section are listed in the bottom part of Table 2. No values of these parameters are reported in the literature.

6 INDIVIDUAL CHEMICAL ABUNDANCES

With a high-resolution HERMES spectrum with an SNR ~100 at hand, it is possible to derive the abundances of chemical elements with a sufficient number of detectable absorption lines in the observed spectrum. We started with an abundance analysis for all the elements assuming local thermodynamic equilibrium (LTE; Section 6.1). Afterwards, we investigated the effect of non-local thermodynamic equilibrium (NLTE) line formation on the abundances for a selection of well-chosen elements (Section 6.2).

6.1 LTE abundance analysis

The individual chemical abundances were calculated via direct fitting of theoretical profiles of individual spectral lines using the $v\sin i$ and $v_{\rm rad}$ values derived in Section 5.1. We used the SYNTHV_NLTE code (Tsymbal et al. 2019) in combination with a grid of pre-computed atmospheric models from the LLmodels package (Shulyak et al. 2004). The calculations were carried out using the IDL visualization program BINMAG6 (Kochukhov 2018). LTE was assumed during spectrum synthesis. We removed the O I triplet around 777.1-5 nm from our abundance analysis since it is affected by non-LTE effects (Przybilla et al. 2000). The line lists and atomic parameters were extracted from the 3D release of the Vienna Atomic Line Database (VALD3; Ryabchikova et al. 2015).

Table 3. Results of the abundance analysis of HD 180347 based on the observed HERMES spectrum and with LTE consideration. Listed in column 2 are the individual chemical abundances inferred for our target star and column 3 gives the solar abundances (Asplund et al. 2009). The number of spectral lines from which the abundances were derived is given between brackets.

Element	$\log(N_{\rm el}/N_{\rm Tot})_*$	$\log(N_{\rm el}/N_{\rm Tot})_\odot$
C	-4.15 ± 0.18 (7)	-3.57
O	-3.97 ± 0.13 (1)	-3.31
Na	-5.42 ± 0.20 (3)	-5.76
Mg	-4.65 ± 0.17 (12)	-4.40
Si	-4.31 ± 0.17 (4)	-4.49
S	-4.62 ± 0.09 (3)	-4.88
K	-7.72 ± 0.13 (1)	-6.97
Ca	-6.45 ± 0.16 (23)	-5.66
Sc	-9.43 ± 0.12 (3)	-8.85
Ti	-7.18 ± 0.15 (23)	-7.05
V	-7.53 ± 0.13 (5)	-8.07
Cr	-6.06 ± 0.13 (13)	-6.36
Mn	-6.44 ± 0.07 (3)	-6.57
Fe	-4.36 ± 0.09 (88)	-4.50
Co	-6.23 ± 0.10 (20)	-7.01
Ni	-5.44 ± 0.10 (16)	-5.78
Cu	-6.98 ± 0.15 (14)	-7.81
Zn	-7.00 ± 0.13 (2)	-7.44
Sr	-7.97 ± 0.12 (4)	-9.13
Y	-9.04 ± 0.14 (5)	-9.79
Zr	-8.93 ± 0.09 (13)	-9.47
Ba	-8.27 ± 0.12 (4)	-9.82
La	-9.48 ± 0.19 (5)	-10.90
Ce	-9.06 ± 0.12 (6)	-10.42
Nd	-9.27 ± 0.12 (9)	-10.58

We divided the HERMES spectrum into several wavelength intervals, each 5 nm wide. We used a χ^2 minimization of the difference between the observed and synthetic spectrum to derive the abundances for each individual line present in the wavelength interval. Table 3 shows the average individual chemical abundances and their uncertainties expressed as $\log(N_{\rm el}/N_{\rm Tot})$. The abundance pattern is shown in relation to solar abundances (Asplund et al. 2009) in Fig. 8. The uncertainties in abundances result from a combined dependence of the errors on $T_{\rm eff}$, $\log g$, $v\sin i$, ξ, the position of the continuum of the normalised HERMES spectrum, and the accuracy of the oscillator strengths ($\log(gf)$) of the lines considered in our analysis. We should be cautious about the abundances of elements whose lines are present in less than three spectral segments because they were calculated from a small number of lines.

Calcium ($\approx$ 0.75 dex) and scandium ($\approx$ 0.6 dex) are found to be underabundant while iron-peak and heavy elements such as strontium, yttrium, zirconium, barium, lanthanum, cerium, praseodymium and neodymium are overabundant. Our abundance analysis reveals a chemical pattern typical for Am stars. As shown in Fig. 9, our abundances are in agreement with those determined by Catanzaro et al. (2015) and Catanzaro et al. (2019).

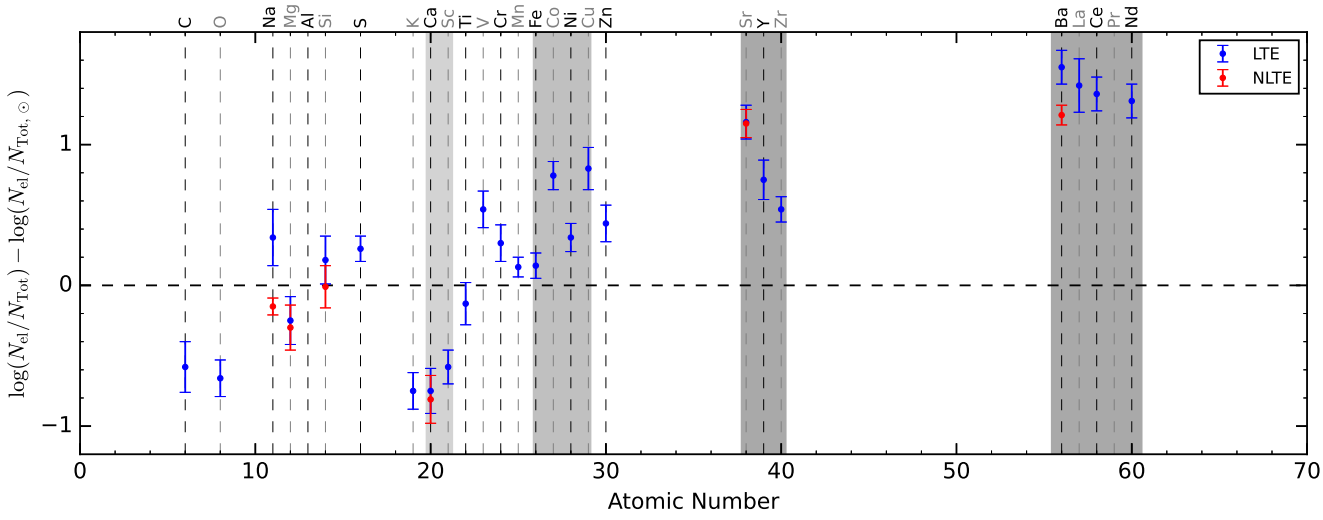

Figure 8. The individual chemical abundance pattern for HD 180347. The horizontal dashed line indicates solar abundances (Asplund et al. 2009). The light elements (Ca and Sc) and heavy elements (Fe, Co, Ni, Cu, Sr, Y, Zr, Ba, La, Ce, Pr, and Nd), important for the classification of Am stars, are highlighted with a gray background. The *blue* and *red* symbols represent the LTE and NLTE abundances, respectively.

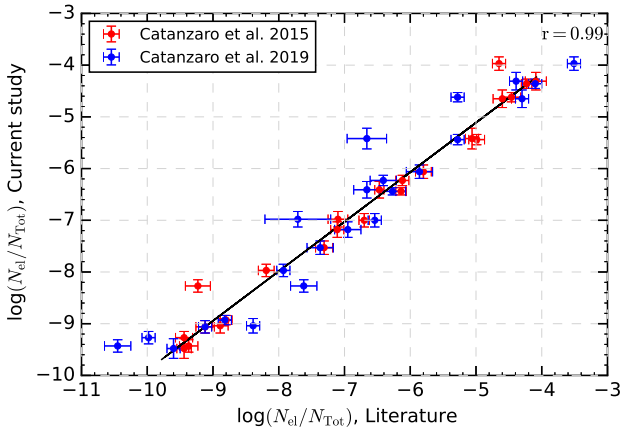

Figure 9. A comparison of our individual chemical abundances with those determined by Catanzaro et al. (2015) and Catanzaro et al. (2019). The corresponding correlation coefficient (r) is given in the top-right corner. For Na, Mg, Si, Ca, Sr, and Ba, we considered NLTE abundances.

for the correct classification of chemically peculiar stars (Preston 1974).

We used the code DETAIL (Giddings 1981; Butler 1984) based on the accelerated Λ-iteration method (Rybicki & Hummer 1991, 1992) to solve the radiative transfer and statistical equilibrium equations. The DETAIL opacity package was updated by Przybilla et al. (2011). The model atoms were produced and described in detail by Alexeeva et al. (2014, Na I), Alexeeva et al. (2018, Mg I-II), Mashonkina (2020, Si I-II), Mashonkina et al. (2007, Ca I-II), and Mashonkina et al. (2020, Sr II, Ba II). We denote the statistical equilibrium and thermal (Saha-Boltzmann) number densities as n_{NLTE} and n_{LTE}, respectively. The obtained departure coefficients ($b = n_{NLTE}/n_{LTE}$) were then used to calculate the synthetic NLTE spectrum with the code SYNTHV_NLTE (Tsymbal et al. 2019). Using the visualization tool BinMag6 (Kochukhov 2018), we compared the synthetic NLTE and observed spectra and performed spectral line fitting. For consistency with the LTE calculations discussed in Section 6.1, we used the same model atmosphere and the line list.

6.2 NLTE abundance analysis

We additionally considered non-local thermodynamic equilibrium (NLTE) line formation for neutral and/or singly-ionised sodium, magnesium, silicon, calcium, strontium, and barium. These elements are some of the most easily observed elements in A-type stars. Magnesium, silicon, and calcium are examples of α-elements. An accurate determination of their abundances is critical for a better understanding of the history of α-process nucleosynthesis in the universe, the formation and evolution of a large number of galaxies, as well as the physics of stars and planetary systems. The α-process is a type of nuclear fusion in which helium is converted into heavier elements in a star (Narlikar 1995). Moreover, having the best possible abundances of calcium, strontium, and barium is also important

The best NLTE fits to the observed Na I 589.592 nm, Mg I 517.285 nm, Si II 637.137 nm, Ca I 643.929, Sr II 421.552 nm, and Ba II 614.171 nm lines are represented with red curves in Fig. 10. The LTE profile (blue curve) was computed for each line using the abundance obtained from the NLTE analysis. Individual line abundances are presented in Tables 4 and 5. Figure 11 shows the differences between the LTE and NLTE abundances (Δ) as a function of wavelength. The average Δ value for lines of Na I, Mg I-II, Si I-II, Ca I-II, Sr II, and Ba II is 0.49 dex, 0.05 dex, 0.19 dex, 0.02 dex, 0.01 dex, and 0.34 dex, respectively. The largest NLTE effects, with Δ exceeding the error limits presented in Table 3, were found for Na I 588.995, 589.592 nm, Mg I 518.360 nm, Mg II 448.115 nm, Si II 634.711, 637.137 nm, Ba II 455.403, 493.408, 614.171, and 649.690 nm.

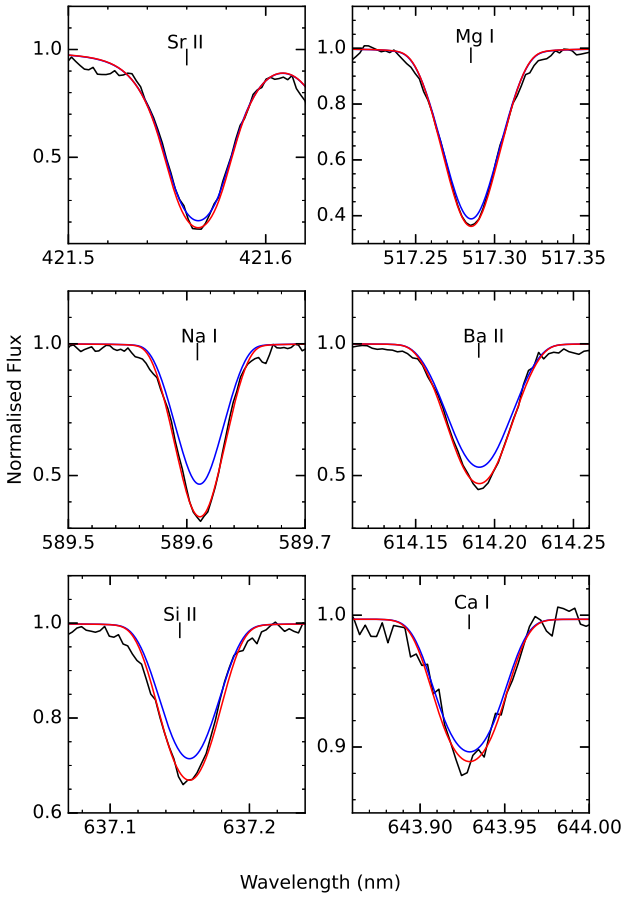

Figure 10. NLTE (*red*) fits of Sr II 421.552 nm, Mg I 517.285 nm, Na I 589.592 nm, Ba II 614.171 nm, Si II 637.137 nm, and Ca I 643.929 nm. For each line, the LTE (*blue*) profile was computed with the respective abundance obtained from NLTE analysis. In each panel, the *black* line represents the observed spectrum.

7 CONCLUSION

In this paper we present a photometric and spectroscopic analysis of HD 180347. The analysis is based on high-precision photometric data by *TESS* and a high-resolution spectrum obtained with HERMES mounted at the Cassegrain focus of the 1.2-m Mercator telescope located at La Palma, Spain. We searched for the variability type, determined the spectral type, and obtained fundamental parameters such as the effective temperature, surface gravity, and projected rotational, microturbulent, and radial velocity. Based on these results, we estimated the radius, equatorial rotational velocity, inclination angle, mass, and age of HD 180347. Finally, we performed a detailed chemical abundance analysis where the differences between the LTE and NLTE calculations are compared for several elements.

Based on the variability analysis of the high-precision photometric data by *TESS* (sectors 14, 15, and 26), we classify HD 180347 as a rotational variable with a period of 4.1 ± 0.2 days. In reference to the observation limit of *TESS*, no pulsations were detected as previously suspected by Catanzaro et al. (2019). Based on the spectral classification analysis and chemical abundance pattern, we classified this star as Am (kA1hA8mA8). NLTE abundance analysis for Na I, Mg I-II, Si I-II, Ca I-II, Sr II, and Ba II indicates an average abundance correction (Δ) of 0.49 dex, 0.05 dex, 0.19 dex, 0.02 dex, 0.01 dex, and 0.34 dex, respectively. We report that Na I 588.995, 589.592 nm, Mg I 518.360 nm, Mg II 448.115 nm, Si II 634.711, 637.137 nm, Ba II 455.403, 493.408, 614.171, and 649.690 nm are more sensitive to NLTE effects.

The availability of HERMES and other spectrographs capable of high-resolution spectroscopy will allow us, in future, to continue with the study of A and probable Am stars especially those reported in Renson & Manfroid (2009). Efforts will be made to increase the number of elements in NLTE abundance analyses.

Table 4. Listed are atomic data for Na I, Mg I/II, and Si I/II lines: the wavelength in nm of the lines used in the analysis, the oscillator strengths ($\log(gf)$) as given in the VALD3 database, the LTE and NLTE abundances, and the abundance correction (Δ). Δ is the difference between LTE and NLTE abundances. LTE means $\log(N_{\rm el}/N_{\rm Tot})_{\rm LTE}$ and NLTE means $\log(N_{\rm el}/N_{\rm Tot})_{\rm NLTE}$.

Wavelength (nm)	$\log(gf)$	LTE	NLTE	Δ
Na I				
568.820	-0.452	-5.70	-5.84	0.14
588.995	0.108	-5.26	-5.90	0.64
589.592	-0.194	-5.29	-5.99	0.70
Mean		-5.42	-5.91	0.49
σ		0.20	0.06	
Mg I				
405.751	-0.900	-4.82	-4.81	-0.01
416.727	-0.745	-4.77	-4.75	-0.02
470.299	-0.440	-4.88	-4.87	-0.01
516.732	-0.931	-4.76	-4.82	0.06
517.285	-0.450	-4.64	-4.76	0.12
518.360	-0.239	-4.25	-4.43	0.18
552.840	-0.498	-4.88	-4.84	-0.04
571.109	-1.724	-4.67	-4.63	-0.04
Mean		-4.54	-4.64	0.03
σ		0.23	0.18	
Mg II				
439.057	-0.53	-4.47	-4.48	0.01
448.115	-0.56	-4.19	-4.44	0.25
787.737	0.39	-4.75	-4.81	0.06
789.637	0.65	-4.73	-4.81	0.08
Mean		-4.71	-4.74	0.10
σ		0.19	0.14	
Si I				
505.598	0.53	-4.24	-4.26	0.02
742.350	-0.176	-4.68	-4.75	0.07
Mean		-4.46	-4.51	0.05
σ		0.22	0.24	
Si II				
634.711	0.17	-4.07	-4.46	0.39
637.137	-0.04	-4.26	-4.53	0.27
Mean		-4.17	-4.50	0.33
σ		0.10	0.04	

ACKNOWLEDGMENTS

The International Science Program (ISP) of Uppsala University and the African Astronomical Society (AfAS) financed the study. The part of the work presented here is supported by the Belgo-Indian Network for Astronomy & Astrophysics (BINA), approved by the International Division, Department of Science and Technology (DST, Govt. of India; DST/INT/Belg/P-02) and the Belgian Federal Science Policy Office (BELSPO, Govt. of Belgium;

Table 5. Similar to Table 4 but for Ca I/II, Sr II, and Ba II lines.

Wavelength (nm)	$\log(gf)$	LTE	NLTE	Δ
Ca I				
401.074	-0.447	-6.17	-6.17	0.00
428.937	-0.233	-6.59	-6.59	0.00
429.899	-0.359	-6.60	-6.60	0.00
445.478	0.258	-6.65	-6.66	0.01
526.170	-0.579	-6.17	-6.16	-0.01
526.224	-0.471	-6.69	-6.69	0.00
526.556	-0.113	-6.09	-6.09	0.00
527.027	0.162	-6.17	-6.20	0.03
558.197	-0.555	-6.41	-6.42	0.01
558.875	0.358	-6.70	-6.71	0.01
559.011	-0.571	-6.33	-6.33	0.00
559.446	0.097	-6.17	-6.20	0.03
585.745	0.240	-6.30	-6.31	0.01
610.272	-0.793	-6.26	-6.29	0.03
612.222	-0.316	-6.61	-6.65	0.04
616.217	-0.090	-6.69	-6.72	0.03
616.956	-0.478	-6.40	-6.42	0.02
643.929	0.390	-6.68	-6.74	0.06
644.981	-0.502	-6.54	-6.58	0.04
646.257	0.262	-6.43	-6.49	0.06
649.378	-0.109	-6.71	-6.74	0.03
714.815	0.137	-6.55	-6.56	0.01
Mean		-6.45	-6.47	0.02
σ		0.21	0.21	
Ca II				
501.997	-0.247	-6.37	-6.38	0.01
Sr II				
407.771	0.143	-8.12	-8.13	0.01
416.179	-0.327	-7.84	-7.86	0.02
421.552	-0.173	-7.87	-7.93	0.06
430.544	-0.041	-8.06	-8.00	-0.06
Mean		-7.97	-7.98	0.01
σ		0.12	0.10	
Ba II				
455.403	-1.447	-8.42	-8.60	0.18
493.408	-1.1	-8.26	-8.57	0.31
614.171	-0.22	-8.33	-8.72	0.39
649.690	-0.521	-8.08	-8.54	0.46
Mean		-8.27	-8.61	0.34
σ		0.12	0.07	

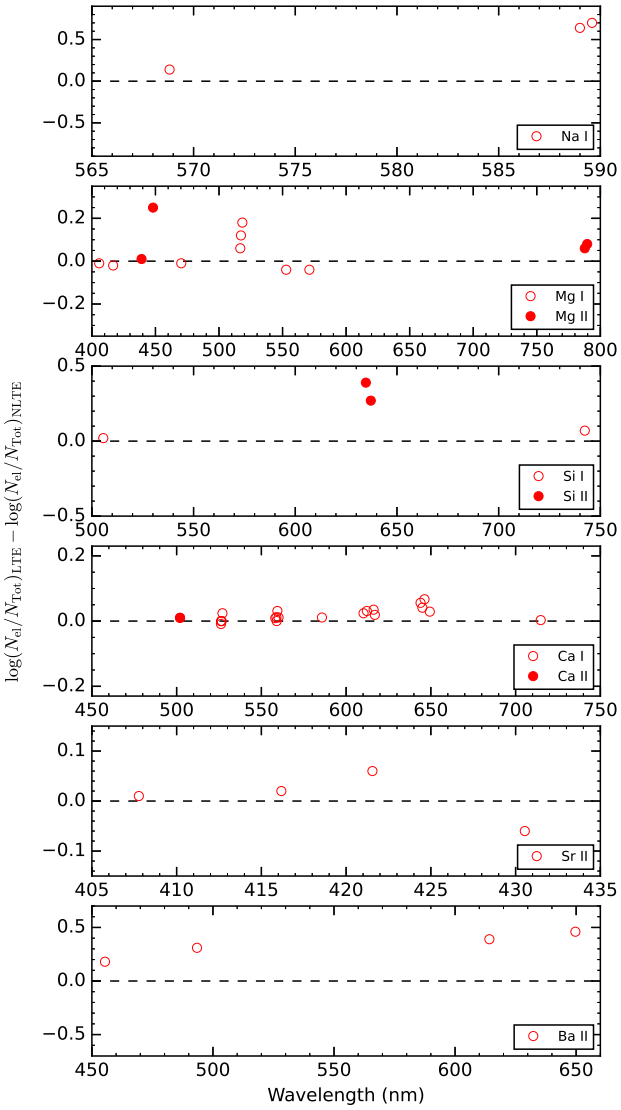

Figure 11. Abundance differences between the LTE and NLTE analyses for Na I, Mg I/II, Si I/II, Ca I/II, Sr II, and Ba II.

BL/33/IN12). Based on observations obtained with the HERMES spectrograph, which is supported by the Research Foundation - Flanders (FWO), Belgium, the Research Council of KU Leuven, Belgium, the Fonds National de la Recherche Scientifique (F.R.S.-FNRS), Belgium, the Royal Observatory of Belgium, the Observatoire de Genève, Switzerland and the Thüringer Landessternwarte Tautenburg, Germany. This publication makes use of VOSA, developed under the Spanish Virtual Observatory project supported by the Spanish MINECO through grant AyA2017-84089. VOSA has been partially updated by using funding from the European Union's Horizon 2020 Research and Innovation Programme, under Grant Agreement 776403 (EXOPLANETS-A). This work has made use of the VALD database, operated at Uppsala University, the Institute of Astronomy RAS in Moscow, and the University of Vienna.

REFERENCES

Abt H. A., 2009, AJ, 138, 28
Aigrain S., et al., 2015, MNRAS, 450, 3211
Alexeeva S., Pakhomov Y., Mashonkina L., 2014, Astronomy Letters, 40, 406
Alexeeva S., Ryabchikova T., Mashonkina L., Hu S., 2018, ApJ, 866, 153
Andrae R., et al., 2018, A&A, 616, A8
Ashoka B. N., et al., 2000, Bulletin of the Astronomical Society of India, 28, 251
Asplund M., Grevesse N., Sauval A. J., Scott P., 2009, ARA&A, 47, 481
Aurière M., et al., 2007, A&A, 475, 1053
Balona L. A., Catanzaro G., Abedigamba O. P., Ripepi V., Smalley B., 2015, MNRAS, 448, 1378
Bayo A., Rodrigo C., Barrado Y Navascués D., Solano E., Gutiérrez R., Morales-Calderón M., Allard F., 2008, A&A, 492, 277
Bidelman W. P., 1985, AJ, 90, 341
Blanco-Cuaresma S., 2019, MNRAS, 486, 2075
Blanco-Cuaresma S., Soubiran C., Jofré P., Heiter U., 2014, in ASInC. (arXiv:1312.4545)
Bohlender D. A., Dworetsky M. M., Jomaron C. M., 1998, ApJ, 504, 533
Boltzmann L., 1884, Annalen der Physik, 258, 291
Borucki W. J., et al., 2010, Science, 327, 977

Bowman D. M., Buysschaert B., Neiner C., Pápics P. I., Oksala M. E., Aerts C., 2018, A&A, 616, A77
Breger M., et al., 1993, A&A, 271, 482
Bressan A., Marigo P., Girardi L., Salasnich B., Dal Cero C., Rubele S., Nanni A., 2012, MNRAS, 427, 127
Browning M. K., Brun A. S., Toomre J., 2004, ApJ, 601, 512
Butler K., 1984, Ph.D. Thesis, University of London
Castelli F., Kurucz R. L., 2003, in Piskunov N., Weiss W. W., Gray D. F., eds, IAU Symposium Vol. 210, Modelling of Stellar Atmospheres. p. A20
Catanzaro G., et al., 2015, MNRAS, 451, 184
Catanzaro G., Busà I., Gangi M., Giarrusso M., Leone F., Munari M., 2019, MNRAS, 484, 2530
Ceillier T., et al., 2015, MNRAS, 456, 119
Ceillier T., et al., 2017, A&A, 605, A111
Conti P. S., 1970, PASP, 82, 781
Costa G., Girardi L., Bressan A., Marigo P., Rodrigues T. S., Chen Y., Lanza A., Goudfrooij P., 2019, MNRAS, 485, 4641
Dziembowski W., Krolikowska M., Kosovichev A., 1988, Acta Astron., 38, 61
Evans D. W., et al., 2018, A&A, 616, A4
Fitzpatrick E. L., 1999, PASP, 111, 63
Flower P. J., 1996, ApJ, 469, 355
Fossati L., Bagnulo S., Landstreet J., Wade G., Kochukhov O., Monier R., Weiss W., Gebran M., 2008, A&A, 483, 891
Frémat Y., Neiner C., Hubert A. M., Floquet M., Zorec J., Janot-Pacheco E., Renan de Medeiros J., 2006, A&A, 451, 1053
Frescura F. A. M., Engelbrecht C. A., Frank B. S., 2008, MNRAS, 388, 1693
García R. A., Mathur S., Salabert D., Ballot J., Régulo C., Metcalfe T. S., Baglin A., 2010, Science, 329, 1032
Gebran M., Monier R., Royer F., Lobel A., Blomme R., 2014, in Mathys G., Griffin E. R., Kochukhov O., Monier R., Wahlgren G. M., eds, Putting A Stars into Context: Evolution, Environment, and Related Stars. pp 193–198 (arXiv:1312.0442)
Giddings J., 1981, Ph.D. Thesis, University of London
Giles H. A. C., Collier Cameron A., Haywood R. D., 2017, MNRAS, 472, 1618
Goupillaud P., Grossmann A., Morlet J., 1984, Geoexploration, 23, 85
Gray R. O., Corbally Christopher J., 2009, Stellar Spectral Classification. Princeton University Press
Gray R. O., Corbally C. J., 2014, AJ, 147, 80
Gray R. O., Corbally C. J., Garrison R. F., McFadden M. T., Robinson P. E., 2003, AJ, 126, 2048
Green G. M., 2018, JOSS, 3, 695
Green G. M., Schlafly E. F., Zucker C., Speagle J. S., Finkbeiner D. P., 2019, arXiv e-prints, p. arXiv:1905.02734
Høg E., et al., 2000, A&A, 357, 367
Holschneider M., Kronland-Martinet R., Morlet J., Tchamitchian P., 1989, in Combes J.-M., Grossmann A., Tchamitchian P., eds, Wavelets. Time-Frequency Methods and Phase Space. p. 286
Hui-Bon-Hoa A., 2000, A&AS, 144, 203
Indebetouw R., et al., 2005, ApJ, 619, 931
Jenkins J. M., et al., 2016, in Software and Cyberinfrastructure for Astronomy IV. p. 99133E
Johnson H. L., Morgan W. W., 1953, ApJ, 117, 313
Jones T. J., Wolff S. C., 1974, PASP, 86, 67
Joshi S., et al., 2003, MNRAS, 344, 431
Joshi S., Mary D. L., Martinez P., Kurtz D. W., Girish V., Seetha S., Sagar R., Ashoka B. N., 2006, A&A, 455, 303
Joshi S., Mary D. L., Chakradhari N. K., Tiwari S. K., Billaud C., 2009, A&A, 507, 1763
Joshi S., Ryabchikova T., Kochukhov O., Sachkov M., Tiwari S. K., Chakradhari N. K., Piskunov N., 2010, MNRAS, 401, 1299
Joshi S., et al., 2012, MNRAS, 424, 2002
Joshi S., et al., 2016, A&A, 590, A116
Joshi S., Semenko E., Moiseeva A., Sharma K., Joshi Y. C., Sachkov M., Singh H. P., Yerra B. K., 2017, MNRAS, 467, 633
Joshi S., et al., 2022, MNRAS, 510, 5854
Kazarovets E., Durlevich O., Kireeva N., Pastukhova E., et al., 2017, Astronomy Reports, 61, 80
Kesseli A. Y., West A. A., Veyette M., Harrison B., Feldman D., Bochanski J. J., 2017, ApJS, 230, 16
Khokhlova V. L., 1981, in Liege International Astrophysical Colloquia. pp 457–463
Kochukhov O., 2018, BinMag: Widget for comparing stellar observed with theoretical spectra (ascl:1805.015)
Koen C., 2010, Ap&SS, 329, 267
Kupka F., Piskunov N., Ryabchikova T. A., Stempels H. C., Weiss W. W., 1999, A&AS, 138, 119
Kurtz D. W., Martinez P., 2000, BaltA, 9, 253
LaSala J., 1994, in Corbally C. J., Gray R. O., Garrison R. F., eds, Astronomical Society of the Pacific Conference Series Vol. 60, The MK Process at 50 Years: A Powerful Tool for Astrophysical Insight. p. 312
Lenz P., Breger M., 2005, CoAst, 146, 53
Martinez P., et al., 2001, A&A, 371, 1048
Mashonkina L., 2020, MNRAS, 493, 6095
Mashonkina L., Korn A. J., Przybilla N., 2007, A&A, 461, 261
Mashonkina L., Ryabchikova T., Alexeeva S., Sitnova T., Zatsarinny O., 2020, MNRAS, 499, 3706
Mathur S., et al., 2010, A&A, 511, A46
Mathur S., et al., 2014, A&A, 562, A124
Mathur S., et al., 2017, ApJS, 229, 30
McDonald I., Zijlstra A. A., Boyer M. L., 2012, MNRAS, 427, 343
McQuillan A., Aigrain S., Mazeh T., 2013, MNRAS, 432, 1203
McQuillan A., Mazeh T., Aigrain S., 2014, ApJS, 211, 24
Michaud G., 1970, ApJ, 160, 641
Montambaux G., 2018, Foundations of Physics, 48, 395–410
Morgan W. W., Keenan P. C., Kellman E., 1943, An atlas of stellar spectra, with an outline of spectral classification. The University of Chicago press
Murphy S. J., 2014, PhD thesis, Jeremiah Horrocks Institute, University of Central Lancashire, Preston, UK <EMAIL>murphy@physics.usyd.edu.au</EMAIL>
Murphy S. J., Hey D., Van Reeth T., Bedding T. R., 2019, Monthly Notices of the Royal Astronomical Society, 485, 2380
Narlikar J., 1995, From Black Clouds to Black Holes. Series in Astronomy and Astrophysics, World Scientific, https://books.google.co.ug/books?id=0_gmjz-L70EC
Oja T., 1985, A&AS, 59, 461
Paul H., Greenberger D. M., Stenholm S. T., Schleich W. P., 2015, Physica Scripta Volume T, 165, 014027
Preston G. W., 1974, ARA&A, 12, 257
Przybilla N., Butler K., Becker S. R., Kudritzki R. P., Venn K. A., 2000, A&A, 359, 1085
Przybilla N., Nieva M.-F., Butler K., 2011, in Journal of Physics Conference Series. p. 012015 (arXiv:1111.1445), doi:10.1088/1742-6596/328/1/012015
Raskin G., et al., 2011, A&A, 526, A69
Renson P., Manfroid J., 2009, A&A, 498, 961
Richer J., Michaud G., Turcotte S., 2000, ApJ, 529, 338
Ricker G. R., et al., 2015, Journal of Astronomical Telescopes, Instruments, and Systems, 1, 014003
Romanyuk I. I., 2007, Astrophysical Bulletin, 62, 62
Ryabchikova T., Piskunov N., Kurucz R. L., Stempels H. C., Heiter U., Pakhomov Y., Barklem P. S., 2015, Physica Scripta, 90, 054005
Rybicki G. B., Hummer D. G., 1991, A&A, 245, 171
Rybicki G. B., Hummer D. G., 1992, A&A, 262, 209
Shulyak D., Tsymbal V., Ryabchikova T., Stütz C., Weiss W. W., 2004, A&A, 428, 993
Skrutskie M. F., et al., 2006, AJ, 131, 1163
Smalley B., et al., 2011, A&A, 535, A3
Smith K. C., 1997, A&A, 319, 928
Sneden C., Bean J., Ivans I., Lucatello S., Sobeck J., 2012, MOOG: LTE line analysis and spectrum synthesis, Astrophysics Source Code Library (ascl:1202.009)
Soufi F., Goupil M. J., Dziembowski W. A., 1998, A&A, 334, 911

Stateva I. K., Iliev I. K., Budaj J., Barzova I. S., 2009, BAJ, 12, 29
Takeda Y., Han I., Kang D.-I., Lee B.-C., Kim K.-M., 2008, Journal of Korean Astronomical Society, 41, 83
Théado S., Vauclair S., Alecian G., LeBlanc F., 2011, in Alecian G., Belkacem K., Samadi R., Valls-Gabaud D., eds, SF2A-2011: Proceedings of the Annual meeting of the French Society of Astronomy and Astrophysics. pp 253–256
Torrence C., Compo G. P., 1998, Bulletin of the American Meteorological Society, 79, 61
Torres G., 2010, The Astronomical Journal, 140, 1158
Trust O., Jurua E., De Cat P., Joshi S., 2020, MNRAS, 492, 3143
Trust O., Jurua E., De Cat P., Joshi S., Lampens P., 2021, MNRAS, 504, 5528
Tsymbal V., Ryabchikova T., Sitnova T., 2019, in Kudryavtsev D. O., Romanyuk I. I., Yakunin I. A., eds, Astronomical Society of the Pacific Conference Series Vol. 518, Physics of Magnetic Stars. pp 247–252
Turcotte S., 2001, arXiv e-prints, pp astro–ph/0111179
Turcotte S., 2003, in Balona L. A., Henrichs H. F., Medupe R., eds, Astronomical Society of the Pacific Conference Series Vol. 305, Magnetic Fields in O, B and A Stars: Origin and Connection to Pulsation, Rotation and Mass Loss. p. 199 (arXiv:astro-ph/0304424)
VanderPlas J. T., 2018, ApJS, 236, 16
Watson W. D., 1970, ApJL, 162, L45
Wenger M., et al., 2000, A&AS, 143, 9
Wright E. L., et al., 2010, AJ, 140, 1868
York D. G., et al., 2000, AJ, 120, 1579

This paper has been typeset from a TEX/LATEX file prepared by the author.